nature communications

Article

https://doi.org/10.1038/s41467-025-67339-7

JULGI coordinates vascular development and leaf patterning through non-cell-autonomous regulation of miR165/166

Received: 3 June 2025

Accepted: 27 November 2025

Published online: 10 January 2026

Check for updates

Soyoung Park[1,3], Hyun Seob Cho[1,3], Seungchul Lee[1], Hojun Lim[1], Chanyoung Park[1], Sangkyu Choi[1], Sang Eun Jun[2], Yoontae Lee[1], Gyung-Tae Kim[2] & Ildoo Hwang[1]

The interplay between vascular development and leaf development is central to the evolutionary success of vascular plants, yet the underlying mechanisms remain poorly understood. Here, we identify the RNA-binding protein JULGI1 (JUL1) as a key integrator of vascular and leaf development in *Arabidopsis*. *JUL1* is transcribed in leaf veins, while the protein distributes throughout the leaf, where it binds G-rich regions of pri-MIR165a transcripts on the abaxial side. This interaction disrupts hairpin formation and inhibits DICER-LIKE1 (DCL1)-mediated processing, reducing miR165/166 levels. Consequently, transcript levels of their targets, the Class III homeodomain leucine zipper (HD-ZIP III), increase, reinforcing adaxial-abaxial polarity. Our findings reveal a non-cell-autonomous mechanism by which vascular-derived JUL1 modulates miRNA biogenesis to coordinate leaf patterning with vascular development.

The leaf is the primary photosynthetic organ of vascular plants, composed of distinct layers, including epidermis, mesophyll, and vasculature, each with unique developmental trajectories and physiological roles[1–3]. Coordinated interactions among these tissues are essential for establishing both the structural framework and functional capacity of the developing leaf. Early vascular plants like Rhyniophytes bore simple, leafless axes containing only vascular strands, and fossil evidence suggests that modern leaves evolved as a secondary innovation through lateral lamina expansion from these strands[4]. This evolutionary trajectory suggests that vascular tissues, beyond resource transport, may have functioned as structural and developmental axes, potentially contributing to leaf polarity and patterning. Developmental evidence supports this link: showing that the asymmetric distribution of specific molecular components establishes polarity, providing positional cues that guide pattern formation during organogenesis[5]. In early leaf development, primary adaxial–abaxial polarity is first established[6–9]. Based on positional information, PIN-FORMED (PIN) auxin efflux transporters direct auxin to accumulate along the central axis of the leaf primordium, where it induces the formation of the provasculature that is subsequently specified and differentiated[10,11]. As a result, the vasculature is formed with its xylem aligned toward the adaxial (upper) side and phloem toward the abaxial (lower) side, reflecting the underlying polarity[12–14]. Subsequently, surrounding tissues undergo coordinated spatial organization and differentiation aligning with the vascular axis and resulting in a pattern that closely mirrors the final geometry of the leaf lamina[10,15]. The frequent occurrence of defective leaf patterning following disruption of vascular patterning[16,17], along with the extensive sharing of key regulatory factors between vascular and leaf development[18–23], suggests their tight interconnection.

Inter-tissue communication is essential for structural organization during organogenesis and is often mediated by non-cell-autonomous regulatory mechanisms[24]. Such regulation requires the production of mobile signaling molecules, their spatially controlled movement between cells or tissues, and the modulation of gene expression in recipient cells. Non-coding RNAs (ncRNAs) have emerged as molecular mediators of this process[25,26], functioning to regulate gene expression or sequester specific transcripts with high specificity and adaptability. In leaf development, abaxially expressed microRNA165/166 (miR165/166) maintains abaxial identity by restricting the activity of class III

[1]Department of Life Sciences, Pohang University of Science and Technology, Pohang, Korea. [2]Department of Molecular Genetics, Dong-A University, Busan, Korea. [3]These authors contributed equally: Soyoung Park, Hyun Seob Cho. e-mail: ihwang@postech.ac.kr

homeodomain leucine zipper (HD-ZIP III) transcription factors[27–29]. Conversely, adaxial miR390 triggers *trans*-acting short-interfering RNA–auxin response factor (tasiR-ARF) biogenesis from adaxially expressed *trans-acting siRNA3* (*TAS3*), leading to degradation of *ARF3/4* transcripts and promoting adaxial growth[30,31]. Their opposing distributions are critical for vascular and leaf patterning. To ensure proper function in response to developmental and environmental cues, ncRNA expression and activity are tightly regulated by multiple protein classes, including transcription factors and RNA-binding proteins, which modulate ncRNA biogenesis, stability, and mobility[32–34]. However, the spatiotemporal mechanisms by which vascular development mediates underlying adaxial-abaxial polarity to shape leaf morphology, particularly through ncRNA regulation to integrate vascular and adjacent tissues during leaf formation, remain largely unknown.

Results

G-rich sequences in primary MIR165 and MIR166 transcripts, key regulators of adaxial–abaxial leaf polarity, may be JUL1 targets

JULGI (JUL) proteins were previously shown to negatively regulate phloem development by binding to G-rich sequences within the 5′ untranslated regions (5′ UTRs) of the *SUPPRESSOR OF MAX2 1-LIKE 4* (*SMXL4*) and *SMXL5* transcripts, which encode positive regulators of phloem differentiation, and suppressing their translation[35–37]. This regulatory mechanism emerged with the evolution of core angiosperms, together with *cis*-acting G-rich elements that facilitate JUL binding[35,38]. These G-rich elements are predicted to form non-canonical secondary structures called RNA G-quadruplexes (RG4s). Notably, in *Arabidopsis*, in silico predictions have identified over 65,000 regions capable of forming RG4s[39], suggesting that JUL1 may have additional roles beyond the translational suppression of *SMXL4* and *SMXL5* transcripts.

Besides their translational regulation, RNA-binding proteins can also regulate RNA processing[40]. Given that ncRNAs are not translated, any interaction between an RNA-binding protein and an ncRNA likely reflects a role in RNA processing. To explore a non-translational role for JUL, we looked for *Arabidopsis* ncRNAs with the putative minimal JUL1-binding sequence, KKGDGGGKW (with K meaning G or U; D meaning any ribonucleotide except C; and W meaning A or U). This sequence was previously identified from Systematic Evolution of Ligands by Exponential Enrichment (SELEX)-enriched sequences (Fig. 1a, top)[35,41]. We detected this sequence in 44 ncRNAs. We separately searched for ncRNAs with G-scores >10, indicating high probability of RG4 formation[42], returning a list of 446 ncRNAs. Of 24 ncRNAs overlapping between these two lists, we ultimately chose five pri-MIR165 and pri-MIR166 transcripts as potential JUL1 targets (Fig. 1a and Supplementary Data 1), given the evolutionary conservation of JUL proteins in core angiosperms and the JUL1-binding sequence in core angiosperms such as black cottonwood (*Populus trichocarpa*, a dicotyledonous tree), *Arabidopsis* (a dicot), and rice (*Oryza sativa*, a monocot) and its absence in the fern *Selaginella moellendorffii* and the moss *Physcomitrium patens* (Fig. 1b and Supplementary Data 2)[35,38,43]. pri-MIRNAs are the primary transcripts from which mature 21–24 nucleotide (nt) miRNAs are produced in plants and animals[44]. Mature miR165/166 molecules regulate adaxial–abaxial patterning by cleaving transcripts encoding HD-ZIP III transcription factors, key regulators of adaxial-side formation in plants[20,23,29,45,46]. *Arabidopsis* has two *MIR165* and seven *MIR166* loci[23,29], producing nine pri-MIR165 or pri-MIR166 transcripts, five of which possess JUL1-binding sequences (Supplementary Data 3). In these pri-MIR165 and pri-MIR166 transcripts, the JUL1-binding sequence and the G-rich elements lie 44 nt from the 5′ end, overlapping with the sequence reverse complementary to mature miR165/166 (Fig. 1c).

To investigate if JUL has additional roles beyond phloem differentiation, we closely examined the morphological changes in *jul* mutants. Notably, we observed markedly altered leaf morphology in the knockout plants, with *jul1* and *jul1 jul2* mutants showing downward-curling, conical leaves (Supplementary Fig. 1a), a typical phenotype of increased abaxial leaf growth in *Arabidopsis*[6,46–48]. To quantify leaf curling, we measured the ratio between visible leaf area and flattened leaf area[49]. This ratio was significantly higher in *jul1* and *jul1 jul2* relative to the wild-type Col-0, and higher in *jul1 jul2* than in *jul1*, suggesting a dosage-dependent effect (Supplementary Fig. 1b). In addition, the *jul1 jul2* mutant showed higher expression of the abaxial marker genes *FILAMENTOUS FLOWER* (*FIL*) and *KANADI* (*KAN*) and lower expression of the adaxial marker genes *PHABULOSA* (*PHB*) and *REVOLUTA* (*REV*) compared to Col-0 (Supplementary Fig. 1c). These data indicate that JUL is involved in leaf adaxial–abaxial patterning.

To determine whether JUL affects the expression of *MIR165/166*, we measured the levels of pri-MIR165a, pri-MIR166a, and mature miR165/166 in Col-0, *jul1*, and *jul1 jul2*. We used pri-MIR166c and pri-MIR166d as internal negative controls that lack the putative minimal JUL1-binding sequence. In *jul1* and *jul1 jul2*, pri-MIR165a and pri-MIR166a levels were lower than in Col-0, whereas those of pri-MIR166c and pri-MIR166d were comparable to Col-0 levels. Mature miR165/166 abundance gradually rose in the order Col-0, *jul1* and *jul1 jul2* (Fig. 1d). These results indicate that pri-MIR165 and pri-MIR166 are likely targets of JUL for the regulation of leaf adaxial–abaxial patterning. To further assess the functional connection between JUL and miR165/166 in leaf adaxial–abaxial patterning, we blocked miR165/166 activity using the Short Tandem Target Mimic (STTM) method[50,51]. Specifically, we expressed STTM165/166, a sequence complementary to miR165/166 but lacking the three central nucleotides, under the control of the meristem-specific *RIBOSOMAL PROTEIN S5* (*RPS5A*) promoter in Col-0 and *jul1 jul2* plants (Supplementary Fig. 2). In the shoot apices of *jul1 jul2 proRPS5A:STTM165/166*, miR165/166 levels were reduced by approximately 40% relative to *jul1 jul2* (Fig. 1e). Whereas the leaves of *jul1 jul2* plants were curled downward and conical-shaped, with a small rosette diameter, *jul1 jul2 proRPS5A:STTM165/166* plants had flattened, round leaves, with a larger rosette diameter, resembling Col-0 plants (Fig. 1f). Additionally, the ratio of curled leaf area to flattened leaf area was lower in *jul1 jul2 proRPS5A:STTM165/166* plants than in *jul1 jul2*, returning to Col-0 levels (Fig. 1g). Consistent with these phenotypic changes, the abaxial marker genes *FIL* and *KAN* were expressed at lower levels, whereas the adaxial marker genes *PHB* and *REV* were more highly expressed, returning to levels similar to Col-0 (Fig. 1h, i). These findings suggest that elevated miR165/166 activity underlies adaxial-abaxial imbalance of *jul1 jul2*, and that JUL modulates miR165/166 levels to maintain adaxial–abaxial patterning.

Vascular bundles in leaves are arranged along the adaxial–abaxial axis, placing xylem on the adaxial side and phloem on the abaxial side[14]. Similar to leaf curling, the more extensive phloem development observed in *jul1 jul2* petioles and inflorescence stems relative to Col-0 returned to Col-0 levels in *jul1 jul2 proRPS5A:STTM165/166* plants (Supplementary Fig. 3a–e). This morphological rescue was associated with lower expression of the phloem marker gene *ALTERED PHLOEM DEVELOPMENT* (*APL*) in *jul1 jul2 proRPS5A:STTM165/166* than in *jul1 jul2*. Notably, the expression levels of the xylem marker gene *XYLEM CYSTEINE PEPTIDASE1* (*XCP1*) and the cambium marker gene *TDIF RECEPTOR* [*TDR*, also reported as *PHLOEM INTERCALATED WITH XYLEM* (*PXY*)] were not significantly different between *jul1 jul2* and *jul1 jul2 proRPS5A:STTM165/166* (Supplementary Fig. 3f). These results suggest that miR165/166 may contribute to JUL-mediated phloem development.

Phloem-derived JUL1 influences leaf adaxial–abaxial patterning via miR165/166

To investigate the spatial expression patterns of *JUL1*, we examined publicly available single-cell RNA-seq datasets from the Leaf SC Atlas[52]. *JUL1* expression was predominantly enriched in cells engaged in the

https://doi.org/10.1038/s41467-025-67339-7

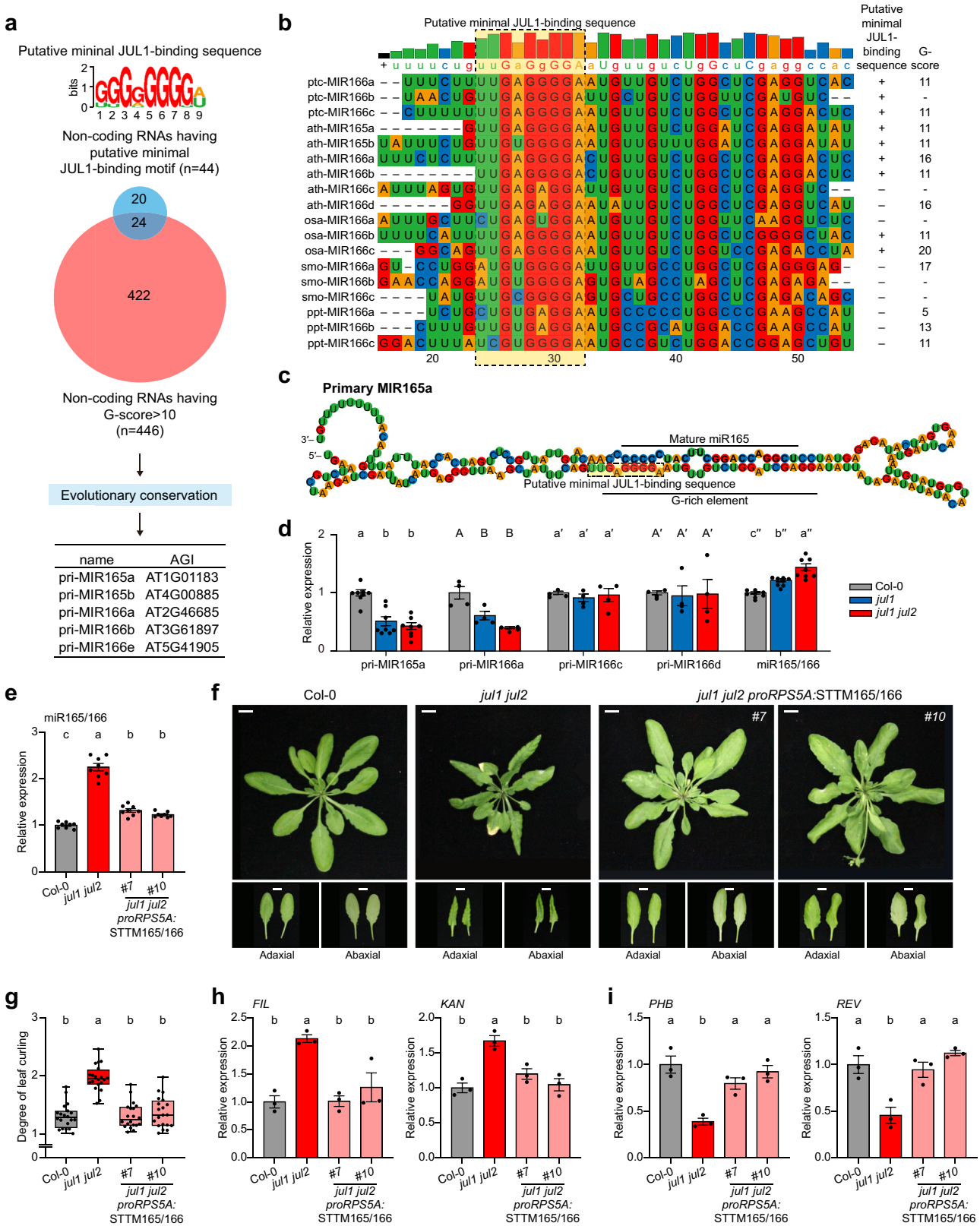

cell cycle, as well as in phloem-related cells, such as companion cells, sieve elements, and phloem parenchyma, where the phloem marker gene *APL* was also expressed. In contrast, *JUL1* transcripts were not detected in abaxial pavement cells, adaxial pavement cells, or guard cells, in which the leaf patterning markers *FIL*, *KAN*, *PHB*, and *PHV* were expressed (Supplementary Fig. 4). To validate the spatial distribution of *JUL1* and pri-MIR165a, we analysed their expression patterns in leaf primordia using green fluorescent protein (GFP) transcriptional fusion lines (*proJUL1:3xGFP* and *proMIR165a:GUS-GFP*) and a translational fusion line (*jul1 jul2 proJUL1:JUL1-GFP*). Consistent with previously published data[28], we detected GFP fluorescence indicative of *MIR165a* transcriptional activity in the abaxial domain of young leaf primordia in *proMIR165a:GUS-GFP* transgenic seedlings (Fig. 2a, b and Supplementary Figs. 5a, e and 6a). By contrast, we observed *JUL1*

Fig. 1 | The G-rich sequences in primary MIR165 and MIR166, key regulators of abaxial-adaxial leaf polarity, are potential targets of JUL1. a Identification of putative JUL1 binding targets in ncRNAs. The putative minimal JUL1-binding sequence was derived from SELEX analysis[35]. The size of each letter designating a nucleotide at each position corresponds to its level of conservation in bits. **b** Consensus sequences of pri-MIR165/166 from various plant species. The putative minimal JUL1-binding sequence in pri-MIR165/166 homologs is conserved across angiosperms. **c** Predicted stem-loop structure of pri-MIR165a. The putative minimal JUL1-binding sequence partially overlaps with the reverse complementary sequence of mature miR165. **d** Relative expression levels of miR165/166 and their primary transcripts in shoot from 7-day-after-sowing (DAS) Col-0, *jul1* and *jul1 jul2* seedlings ($n = 4$ to 8). **e** Relative expression levels of miR165/166 in shoot apices from 7 DAS Col-0, *jul1 jul2*, and *jul1 jul2 proRPS5A:STTM165/166* seedlings ($n = 8$). **f** Representative images of rosette and leaves from 5-week-old Col-0, *jul1 jul2*, and *jul1 jul2 proRPS5A:STTM165/166* plants. Scale bars, 1 cm. **g** Quantification of leaf curling for the transgenic plants described in (**e**). Data are presented as box-and-whisker plots with individual data points ($n = 20$). The centre lines indicate the median, the box limits indicate the 25th percentiles and 75th percentiles, and the whiskers represent the minima and maxima. **h**, **i** Relative expression levels of abaxial (**g**) and adaxial marker genes (**h**) in leaves from 5-week-old Col-0, *jul1 jul2*, and *jul1 jul2 proRPS5A:STTM165/166* plants ($n = 3$). *FIL* and *KAN*, abaxial markers; *PHB* and *REV*, adaxial markers. The bar graphs in **d**, **g**, **h**, and **i** represent the mean ± SEM with individual data points. *n* indicates biological replicates. **d** and **f**–**i** Different letters indicate statistically significant differences ($P < 0.05$), as determined by one-way ANOVA with a post hoc Tukey's HSD test. All experiments were independently repeated three times with consistent results. The data shown are from a representative experimental set.

transcriptional activity specifically in the midvein of leaf primordia in *proJUL1:3xGFP* seedlings (Fig. 2a, b and Supplementary Figs. 5b, f and 6a). Notably, JUL1-GFP accumulated throughout the leaf primordium of *jul1 jul2 proJUL1:JUL1-GFP* seedlings (Fig. 2a, b and Supplementary Figs. 5c, g and 6a). These data suggest that JUL1 may function in a non-cell-autonomous manner, potentially influencing target gene expression beyond the transcriptional domain of its encoding gene.

To test the above notion, we examined whether tissue-specific expression of *JUL1* could rescue the downward-curling, conical leaf phenotype of *jul1 jul2* mutant plants. To this end, we placed *JUL1* transcription under the control of promoters specific to the abaxial region (*FIL*), adaxial region (*BLADE ON PETIOLE 1* [*BOP1*]), or vasculature (*APL*) and introduced each construct into the *jul1 jul2* background (Fig. 2c, d). In all constructs, the *JUL1* coding sequence was cloned in-frame and upstream of the sequence for a StrepII tag. In each case, ectopic *JUL1* expression was sufficient to rescue the mutant leaf phenotype (Fig. 2c, e). Ectopic expression of *JUL1* in the abaxial or vascular domain, driven by the *FIL* or *APL* promoter, respectively, fully restored the leaf phenotype to that seen in Col-0 plants; *JUL1* expression in the adaxial domain driven by the *BOP1* promoter also alleviated the curling phenotype typical of *jul1 jul2*, although to a lesser extent. Leaves of *jul1 jul2 proBOP1:JUL1* plants exhibited more pronounced curling than those of Col-0, *jul1 jul2 proFIL:JUL1*, and *jul1 jul2 proAPL:JUL1* plants. This morphological rescue was accompanied by changes in the expression levels of abaxial marker genes (*FIL*, *KAN*) and adaxial marker genes (*PHB*, *REV*). Compared to Col-0, *jul1 jul2* plants expressed the abaxial marker genes to higher levels and the adaxial marker genes to lower levels. By contrast, these marker genes were expressed at levels comparable to Col-0 in the phenotype-rescued transgenic lines (Fig. 2f, g). Together, these results indicate that JUL1 functions as a non-cell-autonomous regulator of adaxial–abaxial patterning.

JUL1 specifically binds to the G-rich region of pri-MIR165a

To assess whether JUL1 directly binds to pri-MIR165/166, we conducted RNA electrophoretic mobility shift assays (REMSAs). As JUL binds to G-rich elements predicted to form RG4 structures[35], we designed single-stranded RNA probes containing the JUL1-binding sequence (G-block$^{\#1}$) and two adjacent guanine-rich elements (G-block$^{\#2}$ and G-block$^{\#3}$). These sequences have the potential to form RG4 structures in vitro but do not match the canonical RG4-forming motif (5′-$G_{\geq3}N_{1-7}G_{\geq3}N_{1-7}G_{\geq3}N_{1-7}G_{\geq3}$-3′), suggesting a limited propensity for stable RG4 formation (Supplementary Fig. 7). Using GST-tagged JUL1 and GST-JUL1(RA), a dominant-negative form of JUL1 lacking RNA-binding activity[35], we tested binding to the G-rich elements of pri-MIR165a and pri-MIR166a, both of which are affected in *julgi* mutants (Fig. 1d). GST-JUL1 retarded the mobility of both G-rich elements, whereas GST-JUL1(RA) did not (Supplementary Fig. 8b), with JUL1-showing a stronger binding affinity to the G-rich element of pri-MIR165a than pri-MIR166a. Consistent with these results, bead-surface binding assays demonstrated condensation of Cy5-labeled RNA probes at the liquid–solid interface of JUL1-coated beads. Condensation occurred with both probes but was absent with JUL1(RA)-coated beads (Supplementary Fig. 8c). These results demonstrate that both pri-MIR165a and pri-MIR166a can directly interact with JUL1, but because pri-MIR165a exhibited a stronger binding affinity, we focused subsequent analyses on pri-MIR165a.

To further investigate whether JUL specifically binds to the three G-blocks within pri-MIR165a and assess the relative importance of each motif, we generated various G-to-A mutant probes (mut^{ALL}, mut$^{\#1}$, mut$^{\#2}$, and mut$^{\#3}$) in which all G nucleotides within each G-block were changed to A. Recombinant GST-JUL1 caused a mobility shift when incubated with the intact probe, confirming its binding activity, whereas recombinant GST-JUL1(RA) produced no shift (Fig. 3a). GST-JUL1 failed to shift the mut^{ALL} probe, in which all Gs in all three motifs were changed to As. The probes with individually mutated G-blocks (mut$^{\#1}$, mut$^{\#2}$, and mut$^{\#3}$) exhibited weaker shifts than the intact probe, with the strength of residual binding being mut$^{\#3}$, mut$^{\#2}$, and mut$^{\#1}$ from highest to lowest binding (Fig. 3a, b). To better pinpoint the binding site of JUL1 within pri-MIR165a, we conducted REMSA using radiolabelled probes and unlabelled (cold) competitors. Recombinant GST-JUL1 binding to intact radiolabelled probes was disturbed by increasing amounts of cold competitor probes. The intact probe showed the strongest competition capacity, whereas mut^{ALL} failed to disturb the protein–probe interaction when incubated with the intact probe or the full-length pri-MIR165a (Fig. 3c, d and Supplementary Fig. 8d, e). The competition capacity of the G-block mutants was highest for mut$^{\#3}$, followed by mut$^{\#2}$ and mut$^{\#1}$. These results demonstrate that JUL1 directly binds to three distinct G-blocks within the G-rich elements of pri-MIR165a. Although each G-block contributes differently to the binding affinity, all G-blocks are required for JUL1-binding.

To further examine the association between JUL1 and pri-MIR165a, we turned to an RNA monitoring system based on the hairpin from bacteriophage MS2 and MS2 coat protein in *Arabidopsis* protoplasts[35,53]. Accordingly, we appended 24 copies of the MS2 hairpin to full-length pri-MIR165a, enabling direct visualization of pri-MIR165a via binding of GFP-tagged MS2 coat protein in vivo. We co-transfected this RNA monitoring system into *Arabidopsis* protoplasts with a construct encoding mRFP-tagged JUL1 or mRFP-JUL1(RA). We observed co-localization of MS2-GFP with cytoplasmic compartments of mRFP-JUL1 when pri-MIR165a was fused with MS2 hairpins, but not with mRFP-JUL1(RA) (Fig. 3e, f), indicating that JUL1 associates with pri-MIR165a. Next, we performed an RNA immunoprecipitation (RIP) assay to directly assay the interaction between JUL1 and pri-MIR165a, using anti-HA antibodies on leaf extracts from Col-0 and two *jul1 proJUL1:JUL1-HA* complementation lines. Compared to Col-0, pri-MIR165a was highly enriched in the immunoprecipitates from *jul1 proJUL1:JUL1-HA* leaves, confirming the specific association of JUL1 with pri-MIR165a in vivo (Fig. 3g). Taken together, these results indicate that JUL1 directly binds to the G-rich region of pri-MIR165a in vitro and *in planta*.

https://doi.org/10.1038/s41467-025-67339-7

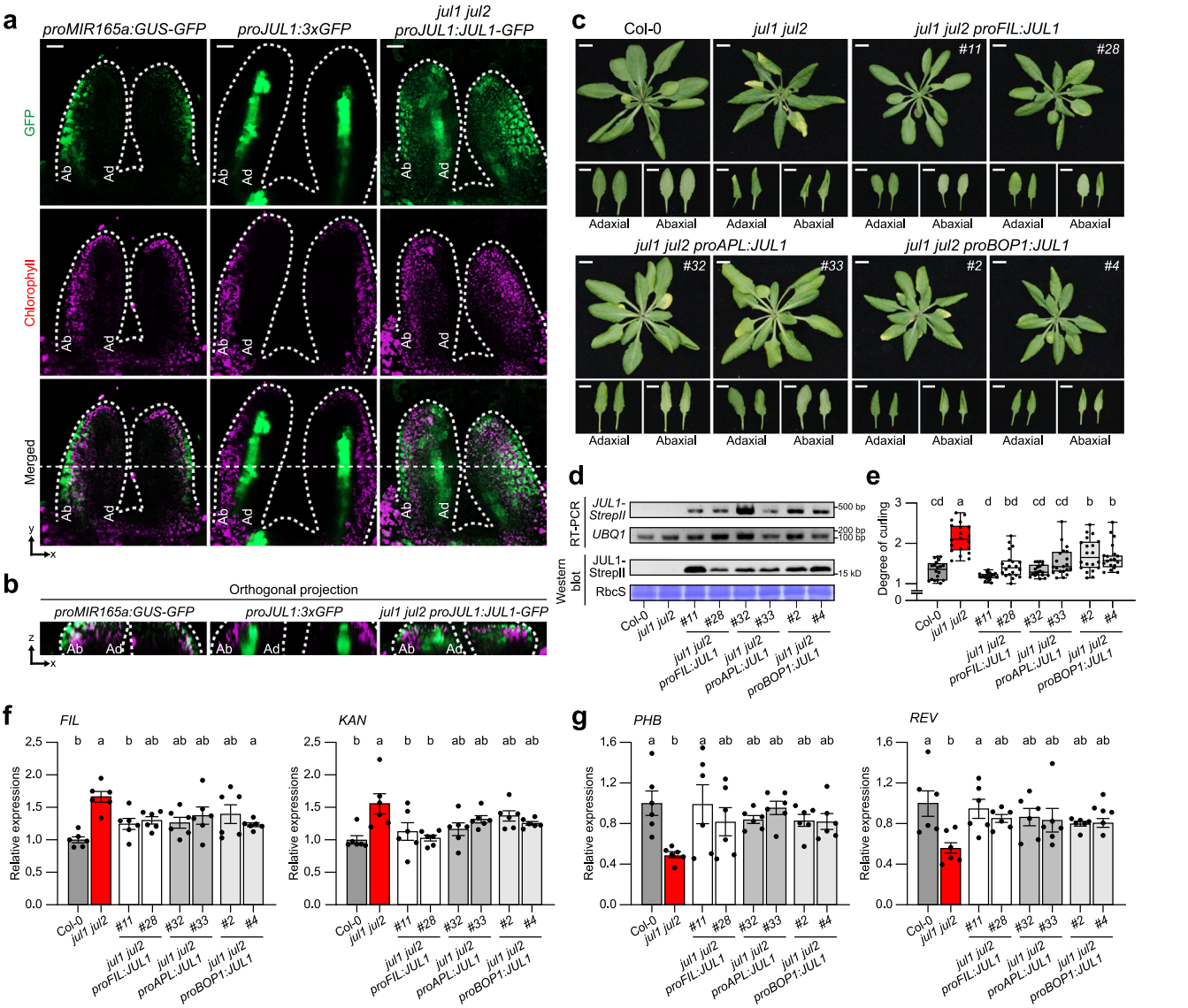

Fig. 2 | Phloem-derived JULGI is involved in leaf abaxial-adaxial patterning via miR165/166. a Longitudinal images from emerging leaf primordia 1st and 2nd true leaves of 4 DAS *proMIR165a:GUS-GFP* (left), *proJUL1: 3xGFP* (middle), and *jul1 jul2 proJUL1:JUL1-GFP* (right) seedlings, respectively. Scale bars, 20 μm. ad, adaxial; ab, abaxial. **b** Orthogonal projection images of the dashed-line positions of (**a**). ad, adaxial; ab, abaxial. **c** Representative images of rosettes and individual leaves from 5-week-old Col-0, *jul1 jul2*, *jul1 jul2 proFIL:JUL1*, *jul1 jul2 proAPL:JUL1*, and *jul1 jul2 proBOP1:JUL1*. Scale bars, 1 cm. **d** *JUL1-StrepII* mRNA and JUL1-StrepII protein were determined from Col-0, *jul1 jul2*, *jul1 jul2 proFIL:JUL1*, *jul1 jul2 proAPL:JUL1*, and *jul1 jul2 proBOP1:JUL1* using RT-PCR and immunoblotting. RbcS protein was used as the loading control. **e** Quantification of leaf curling for the transgenic plants described in (**c**). Data are presented as box-and-whisker plots with individual data points ($n = 20$). The centre lines indicate the median, the box limits indicate the 25th percentiles and 75th percentiles, and whiskers represent the minima and maxima. Relative expression levels of abaxial (**f**) and adaxial (**g**) marker genes in Col-0, *jul1 jul2*, *jul1 jul2 proFIL:JUL1*, *jul1 jul2 proAPL:JUL1*, and *jul1 jul2 proBOP1:JUL1* ($n = 6$). *FIL* and *KAN*, abaxial marker genes; *PHB* and *REV*, adaxial marker genes. The bar graphs in **f** and **g** represent the mean ± SEM with individual data points. *n* indicates biological replicates. **e**–**g** Different letters indicate statistically significant differences ($P < 0.05$), as determined by one-way ANOVA with a post hoc Tukey's honest significant difference (HSD) test. All experiments were independently repeated three times with consistent results. The data shown are from a representative experimental set.

JUL1 inhibits DCL1-mediated processing of pri-MIR165a

In the *jul1* and *jul1 jul2* mutants, pri-MIR165a levels were lower, whereas those of mature miR165/166 were higher (Fig. 1d), suggesting that JUL1 is involved in miRNA processing. During the processing of pri-MIRNA transcripts into mature miRNAs, DICER-LIKE 1 (DCL1) typically recognizes and cleaves hairpin-structured double-stranded pri-MIRNAs, producing a 21-bp miRNA/miRNA* duplex[54,55]. However, JUL1 is thought to bind single-stranded RNA through its RanBP2-type zinc finger (ZnF) domains[35,56].

To explore whether JUL1 binding to pri-MIR165a prevents the formation of double-stranded (ds) RNA, we employed a bead surface binding system that captures a Cy3-labelled anti-probe onto streptavidin beads coated with a biotinylated, Cy5-labelled probe corresponding to the entire G-rich element with all three G-blocks. Beads coated with the probe were surrounded by red signal under confocal microscopy, and co-incubation with the anti-probe produced a green fluorescence signal in the absence of JUL1, indicative of dsRNA formation (Fig. 4a). Importantly, the Cy3 green signal intensity was much lower in the presence of JUL1, suggesting diminished co-localization of the probe and anti-probe or dsRNA formation. By contrast, fluorescence signals in the presence of JUL1(RA) were comparable to those in the absence of JUL1. Subsequently, we conducted Förster resonance

https://doi.org/10.1038/s41467-025-67339-7

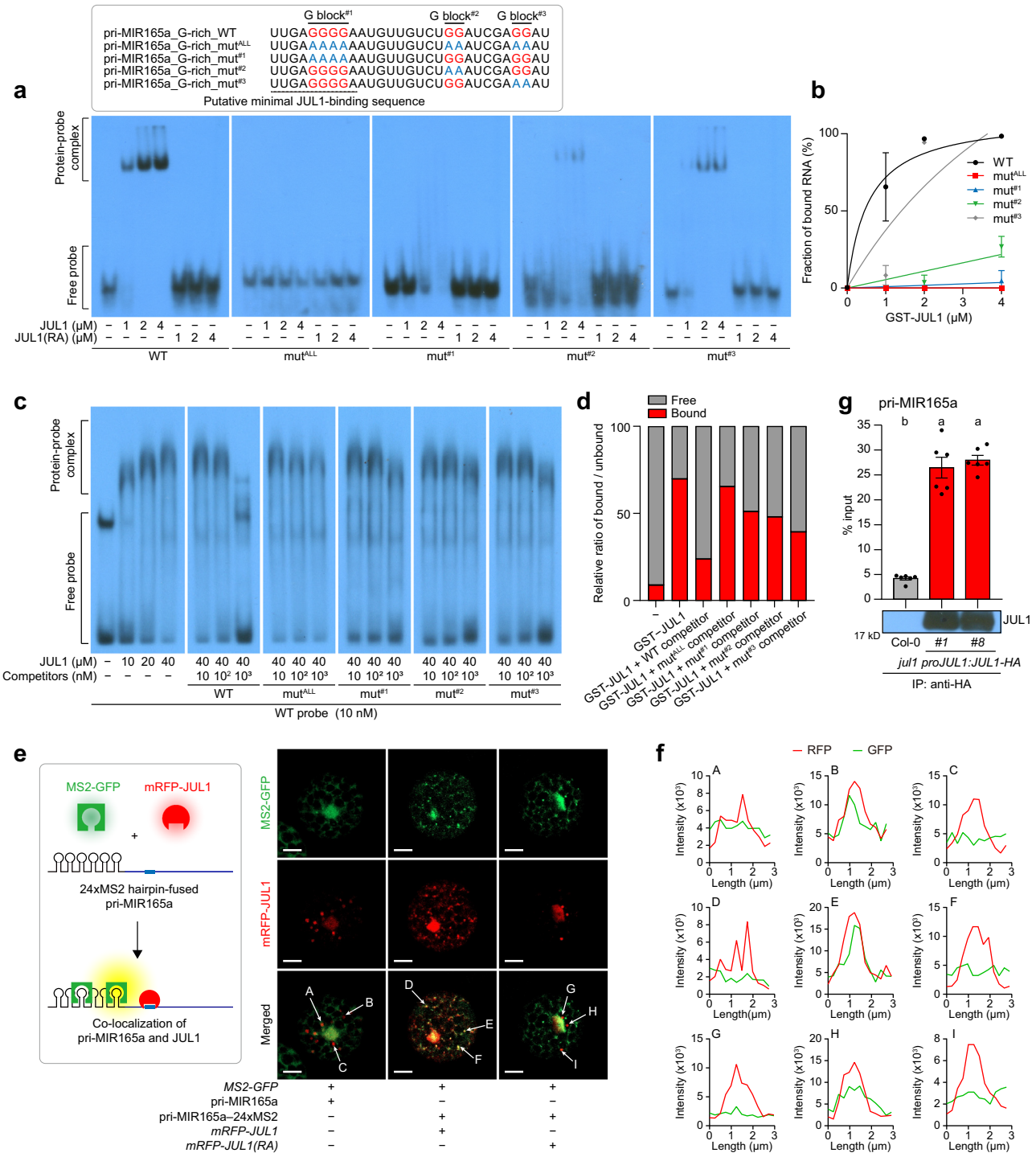

Fig. 3 | JUL1 specifically binds to the G-rich region of pri-MIR165a. a REMSA of the G-rich element within pri-MIR165a and its mutant variants with GST-JUL1 and GST-JUL1(RA) at increasing protein concentrations. The G-rich element contains three G blocks. Blue letters indicate G to A substitutions. **b** Quantification of probe-JUL1 binding shown in (**a**). The *Y*-axis shows the percentage of JUL1 bound probe relative to the total probe, and the *X*-axis indicates JUL1 concentration. Band intensities were measured using ImageJ. **c** REMSA of full-length pri-MIR165a with GST-JUL1 in the presence of increasing amounts of various cold competitors. **d** Quantification of JUL1 binding shown in (**c**). The relative ratio of protein-probe complex to free probe is presented. Band intensities were determined using ImageJ. **e** Co-localization of pri-MIR165a with JUL1 proteins in Arabidopsis protoplasts. (Left) Schematic diagram of the MS2 coat protein/24×MS2 hairpin system fused to pri-MIR165a for in vivo visualization. (Right) MS2-GFP signals represent the localization of MS2 coat protein which profile MS2 hairpin-fused pri-MIR165a, and mRFP signals show the cellular distributions of JUL1 or JUL1(RA). Scale bars, 10 μm. **f** Intensity profiles of GFP (MS2) and RFP (JUL1) fluorescence in the cytosolic compartment indicated by arrows in **e**. **g** Association of JUL1 with pri-MIR165a *in planta*. JUL1 was immunoprecipitated with an anti-HA antibody from 4-week-old Col-0 and *jul1 proJUL1:JUL1-HA* leaves. JUL1 proteins and pri-MIR165a transcripts were determined by immunoblot and qRT-PCR, respectively. Enrichment values of pri-MIR165a were normalized to % input. The bar graph represents the mean ± SEM with individual data points ($n = 6$, biological replicates). Different letters indicate statistically significant differences ($P < 0.05$), as determined by one-way ANOVA with a post hoc Tukey's HSD test. All experiments were independently repeated three times with consistent results. The data shown are from a representative experimental set.

https://doi.org/10.1038/s41467-025-67339-7

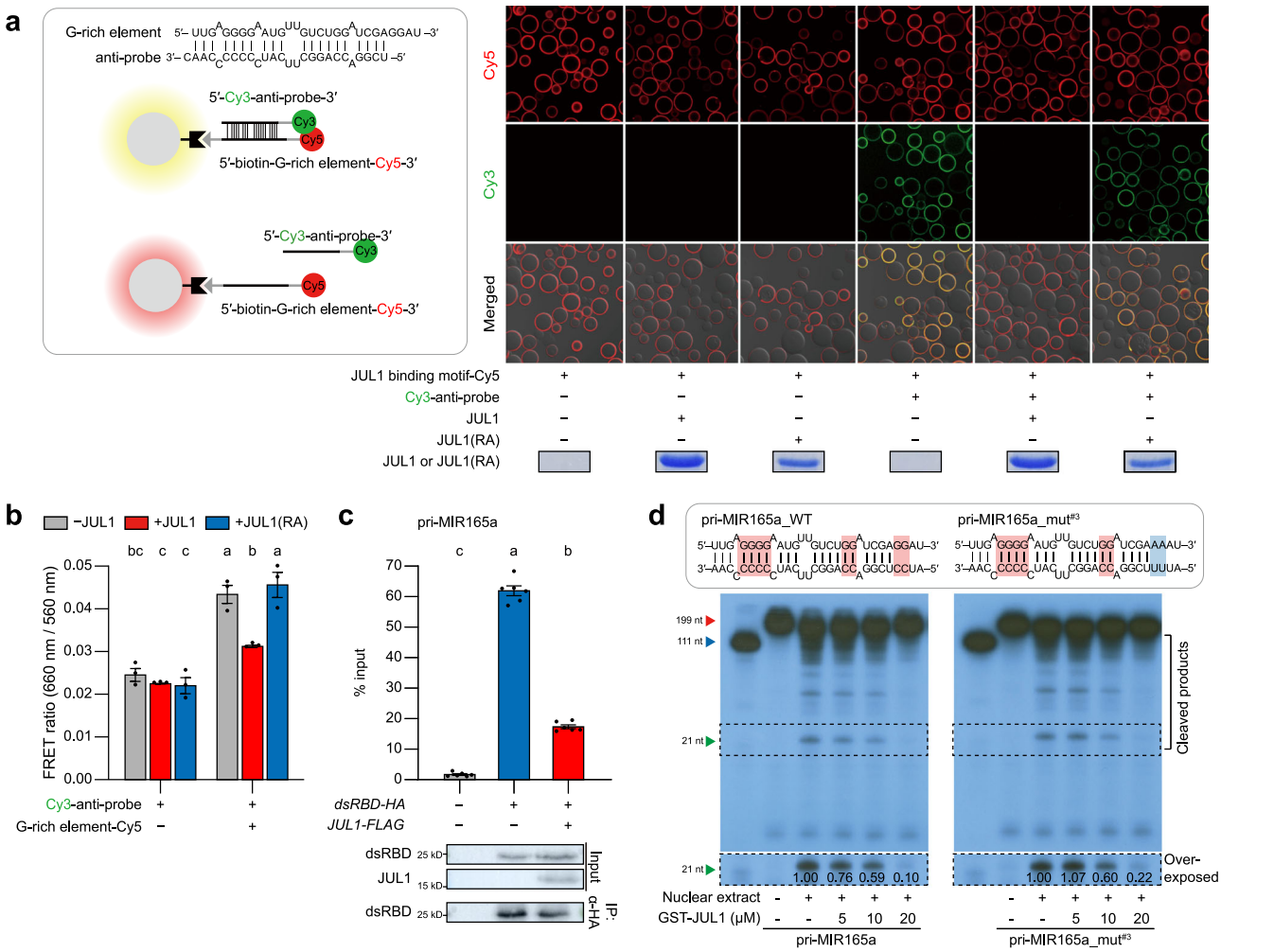

Fig. 4 | Direct binding of JUL1 to pri-MIR165a inhibits DCL1-mediated processing. a Bead-binding assay for interaction between the G-rich element and its antisense counterpart (anti-probe) in the presence of GST-JUL1 or GST-JUL1(RA). The schematic diagram illustrates the setup: G-rich element-coated streptavidin beads were incubated with or without the anti-probe and GST-JUL1. The G-rich element is Cy5-labeled (red fluorescence), while the anti-probe is Cy3-labeled (green fluorescence). Hybridization of the anti-probe and the G-rich element, mediated by Watson-Crick base pairing, is depicted by a yellow fluorescence signal. **b** Förster resonance energy transfer (FRET) analysis using Cy5-labeled G-rich element and Cy3-labeled anti-probe in the presence of GST-JUL1 or GST-JUL1(RA) ($n = 3$). The fluorescence intensities of Cy3 and Cy5 were measured at 560 nm and 660 nm, respectively, with an excitation at 520 nm. **c** Altered association of DCL1 with pri-MIR165a by JUL1 ($n = 6$). In protoplasts, pri-MIR165a was co-expressed with the dsRNA-binding domain of *DCL1* (*dsRBD-HA*), either alone or together with *JUL1-FLAG*. dsRBD-HA was immunoprecipitated with an anti-HA antibody, and the associated levels of pri-MIR165a were determined by qRT-PCR. **d** In vitro pri-MIR165a processing assay performed with isolated nuclei from *YFP-DCL1* expressing protoplasts. Nuclear protein extracts were incubated with pri-MIR165a in the presence of increasing amounts of GST-JUL1. Red, blue, and green sequences indicate G blocks, mature miR165, and mutated nucleotides, respectively. Red, blue, and green arrowheads denote the primary, precursor, and mature forms of pri-MIR165a, respectively. The bar graphs in b and c represent the mean ± SEM with individual data points. *n* indicates biological replicates. Different letters indicate statistically significant differences ($P < 0.05$), as determined by two-way ANOVA with a post hoc Tukey's HSD test (**b**) and one-way ANOVA with a post hoc Tukey's HSD test (**c**). All experiments were independently repeated three times with consistent results. The data shown are from a representative experimental set.

energy transfer (FRET) analysis using the entire G-rich element (labelled with Cy5) and the anti-probe (labelled with Cy3) in the presence of JUL1 or JUL1(RA) (Fig. 4b). When we added the Cy5-labelled probe to the Cy3-labelled anti-probe, the FRET ratio rose in the absence of JUL1 and in the presence of JUL1(RA). However, the FRET ratio was significantly lower in the presence of JUL1 relative to the absence of JUL1 or the presence of JUL1(RA). These findings support the notion that JUL1 impedes hairpin-loop dsRNA formation by binding to single-stranded pri-MIR165a.

To investigate if JUL1 affects the interaction between pri-MIR165a and the dsRNA-binding domain (dsRBD) of DCL1, we conducted native RIP assays for pri-MIR165a using the dsRBD of DCL1 conjugated to an HA tag (dsRBD-HA) in the presence or absence of FLAG-tagged JUL1 (JUL1-FLAG). In protoplasts co-expressing *JUL1-FLAG*, pri-MIR165a levels co-immunoprecipitated with dsRBD-HA were significantly lower than those obtained in the absence of JUL1 (Fig. 4c). To confirm whether JUL1 impairs DCL1 activity toward pri-MIR165a, leading to its diminished processing into mature miR165, we conducted an in vitro pri-MIRNA processing assay. We used radiolabelled pri-MIR165a_WT and its mutant form pri-MIR165a_mut$^{\#3}$, to which JUL1 has a lower binding affinity, without altering the target specificity of mature miR165a. We performed the assay using nuclear extracts from *Arabidopsis* protoplasts overexpressing *YFP-DCL1*, along with increasing amounts of recombinant GST-JUL1 added to the extracts. Nuclear extract facilitated the production of a 21-nt mature miR165 from both the 199-nt pri-MIR165a_WT and pri-MIR165a_mut$^{\#3}$ (Fig. 4d). With more GST-JUL1 added, the abundance of processed miR165a from pri-MIR165a_WT diminished; however, pri-MIR165a_mut$^{\#3}$ was associated

with a weaker suppression of mature miR165 production than pri-MIR165a_WT, at an identical concentration of GST-JUL1, indicating that JUL1 reduces the efficiency of DCL1-mediated processing of pri-MIR165a into mature miR165. Collectively, these results suggest that JUL1 interferes with the incorporation of pri-MIR165a into the dsRNA-binding domain of DCL1, possibly through competitive binding or steric hindrance, thereby suppressing miR165a biogenesis.

JUL1 regulates leaf adaxial–abaxial growth by suppressing miR165/166 levels

To establish the effects of JUL1 on miR165a biogenesis and its downstream targets, we co-transfected pri-MIR165a into *Arabidopsis* protoplasts with *GFP* reporters harbouring the GFP coding sequence cloned in-frame and downstream of the intact miR165/166-binding site of *PHB* transcripts (*PHBBS-GFP*) or a mutant in the miR165/166-binding site (*mPHBBS-GFP*)[45,46] with *JUL1* or *JUL1*(*RA*). In protoplasts expressing the *PHBBS-GFP* reporter, we observed JUL1-dependent increases in pri-MIR165a levels, *PHBBS-GFP* transcripts and GFP signals, concomitant with lower levels of mature miR165/166 (Fig. 5a, top). By contrast, in protoplasts expressing the *mPHBBS-GFP* reporter, *GFP* transcripts and GFP signals remained constant regardless of the amount of JUL1 added, whereas pri-MIR165a abundance rose and that of mature miR165/166 diminished in a JUL1-dependent manner. Unlike JUL1, JUL1(RA) did not affect mature miR165/166 levels, nor did it influence *GFP* transcript or GFP levels in protoplasts expressing either *PHBBS-GFP* or *mPHBBS-GFP* (Fig. 5a, bottom). To exclude the possibility that the observed phenotypic changes in *jul1* and *jul1 jul2* indirectly affect miR165/166 levels and to clarify the specific role of JUL1 in miR165/166 biogenesis, we assessed the abundance of pri-MIR165a, mature miR165/166, and the miR165/166 target transcripts *PHB* and *REV* in lines with *JUL1*-inducible expression in the *jul1* background (*jul1 LhGR-JUL1*) and *JUL1*-inducible knockdown in the Col-0 background using an artificial microRNA (*LhGR*-amiR-*JUL1*). Compared to mock-treated seedlings, dexamethasone (DEX)-treated *jul1 LhGR-JUL1* seedlings showed significantly higher levels of *JUL1* transcripts and pri-MIR165a and lower levels of mature miR165/166 (Fig. 5b). Consistent with the lower miR165/166 levels, *PHB* and *REV* transcript levels were significantly higher in DEX-treated seedlings than in mock-treated seedlings. By contrast, DEX treatment of *LhGR*-amiR-*JUL1* seedlings resulted in markedly lower levels of *JUL1*, *PHB* and *REV* transcripts and pri-MIR165a, alongside greater abundance of mature miR165/166 (Fig. 5c). These findings suggest that the curled-leaf phenotype and altered miR165/166 abundance in *jul1 jul2* plants can be directly attributed to the regulatory role of JUL toward miRNA abundance, rather than secondary effects caused by greater phloem and abaxial development.

To further investigate the roles of JUL in miR165/166 biogenesis during leaf adaxial–abaxial patterning, we introduced the constructs *proMIR165a:MIR165a_WT* and *proMIR165a:MIR165a_mut*$^{\#3}$ individually into Col-0 and *jul1 jul2*. In the Col-0 background, *proMIR165a:MIR165a_WT* transgenic plants developed rosettes and leaves comparable to those of Col-0, with a similar degree of curling. By contrast, *proMIR165a:MIR165a_mut*$^{\#3}$ lines exhibited significant downward leaf curling, indicating more pronounced abaxial growth (Fig. 5d, e). Notably, the curling phenotype in *proMIR165a:MIR165a_mut*$^{\#3}$ in the Col-0 background closely resembled that of *jul1 jul2*. However, in the *jul1 jul2* background, neither transgene further altered leaf morphology beyond the *jul1 jul2* phenotype. To confirm that the curly leaf phenotype was associated with JUL-dependent miR165/166 biogenesis, we measured pri-MIR165a and miR165/166 levels. Both *proMIR165a:MIR165a_WT* and *proMIR165a:MIR165a_mut*$^{\#3}$ transgenes led to higher abundance of mature miR165/166 in all lines compared to their respective backgrounds (Supplementary Fig. 9). However, the ratio of mature miR165/166 to pri-MIR165a, an indicator of processing efficiency, was significantly higher in *proMIR165a:MIR165a_mut*$^{\#3}$ than in its wild-type Col-0, whereas the ratio in *proMIR165a:MIR165a_WT* was similar to that in Col-0 (Fig. 5f). By contrast, we observed no significant differences in this ratio in *jul1 jul2* or its derived transgenic lines. These results indicate that JUL1-binding to pri-MIR165a is crucial for suppressing miR165/166 processing and that disruption of this interaction leads to enhanced miR165/166 biogenesis and thus to leaf curling.

Discussion

The vascular system, composed of phloem, xylem, and supporting non-conducting tissues, is the primary conduit for water, nutrients, and photosynthates[57]. In leaves, veins must both deliver water and minerals to photosynthetically active leaf cells and export sugars, necessitating tight coordination between vascular development and leaf growth. Vascular differentiation must factor into the growth dynamics of surrounding tissues to ensure seamless structural integration during organ formation, and interlayer communication is essential for structural and functional integrity in organogenesis. Here, we propose that the RNA-binding protein JUL1 is intercellular signalling factor coordinating leaf and vascular development, supporting a model in which the vasculature functions as a structural axis to refine leaf polarity during leaf development.

In the early stage of leaf development, the polarized distribution of adaxial–abaxial mediators provides positional cues for cell fate specification and differentiation. In the abaxial domain, miR165/166 maintains abaxial identity by repressing HD-ZIP III, the key determinants of adaxial fate[7–9]. With the onset of phloem development in the midvein of leaf primordia, JUL1 is initially expressed in the midvein and subsequently distributed to neighboring tissues. Vascular-derived JUL1 feeds back to modulate the polar distribution of the miR165/166–HD-ZIP III module, which recalibrates adaxial-abaxial polarity and subsequent patterning. This feedback ensures that the adaxial–abaxial leaf patterning remains coordinated with the extent of vascular pattern, thereby preserving structural and developmental integration of these tissues. Mechanistically, this process parallels the action of ARGONAUTE10 (AGO10), as both limit miR165/166 activity through post-transcriptional regulation[58,59]. Whereas AGO10, ASYMMETRIC LEAVES1/2[60], and HD-ZIP II[28] act in the adaxial domain to restrict miR165/166 accumulation, JUL1 acts in the abaxial domain to modulate miR165/166 biogenesis. Thus, JUL1 fine-tunes the abaxial source strength of miR165/166, adding a distinct layer of spatial regulation to the polarity network. Furthermore, *JUL1* and pri-MIR165a are both expressed in the shoot apical meristem and young developing leaves, but their expression gradually diminishes as leaves mature (Supplementary Fig. 6b). The proximal-to-distal expression pattern of *JUL1* and pri-MIR165a suggests their involvement in developing tissues and reflects their continuous role in optimizing leaf patterning throughout leaf development.

The evolutionary relationships among these factors support roles of JUL1 and possibly JUL2 as developmental coordinators. The miR165/166–HD-ZIP III module emerged early in land plant evolution to regulate polarity-based development. In moss, this module regulates leaf-like organ, phyllid, patterning and asymmetrical cell division in the meristem[61,62], suggesting an early evolutionary role in polarity-based development. This miR165/166–HD-ZIP III module was selected early in land plant evolution[63] and has been conserved in vascular plants to direct organ patterning in roots, stems and leaves[22,27,28,64,65]. JUL appears to have been co-opted as a molecular regulator to coordinate pre-emerged vasculature and newly developed leaf tissues during this evolutionary transition. The G-rich elements recognized by JUL are conserved within pri-MIR165/166 transcripts across diverse plant taxa (Fig. 1b). JUL homologs are conserved throughout vascular plants and even found in some nonvascular species[35,38]. However, JUL homologs in nonvascular species failed to recover the developmental defects in *jul1 jul2*, implying that their regulatory function via association of G-rich elements has been established after the emergence of vascular plants. These evolutionary relationships suggest that the integration of JUL

https://doi.org/10.1038/s41467-025-67339-7

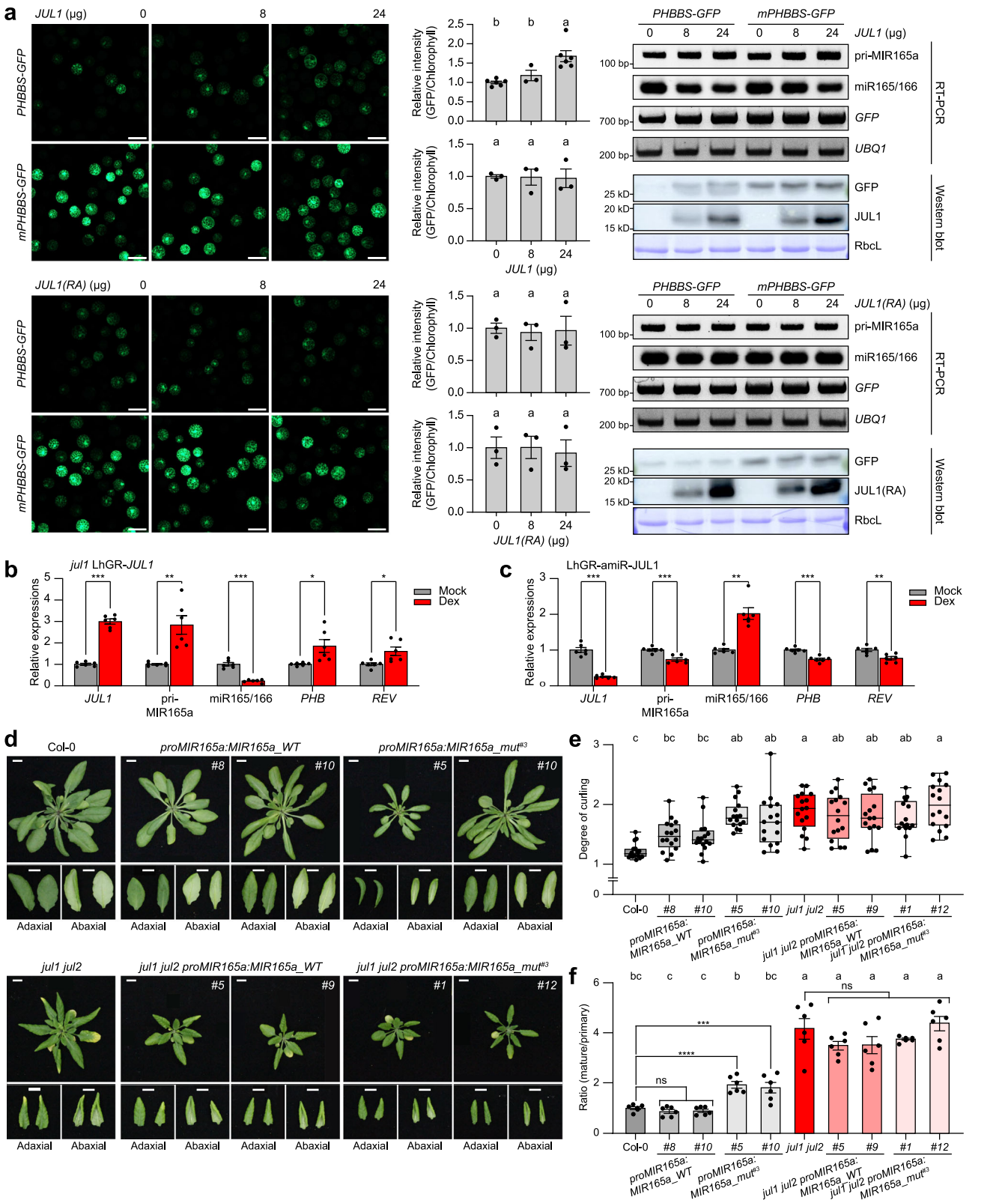

into the miR165/166–HD-ZIP III module represents an evolutionary innovation enabling coordinated tissue patterning in vascular plants.

Leaf patterning is highly correlated with photosynthetic efficiency[66]. The flattened leaf enhances photosynthetic efficiency by increasing surface area for light absorption. *JUL1* is transcriptionally responsive to sucrose[35], suggesting that it may link photosynthetic efficiency with patterning cues during leaf development. We propose that the JUL–miR165/166 module senses photosynthetic status and modulates leaf development accordingly. Under photosynthetically favourable conditions, elevated sugar levels induce *JUL1* expression, which limits abaxial identity while promoting adaxial expansion, ultimately facilitating flatter leaf formation for efficient photosynthesis. In this framework, JUL1 exemplifies a mobile, vascular-derived regulator linking intrinsic developmental patterning with extrinsic

Fig. 5 | JUL1 refines leaf adaxial-abaxial patterning by suppressing miR165/166 levels in the abaxial domain. a Representative images and relative GFP intensities of *Arabidopsis* protoplasts expressing *GFP* conjugated to the intact or mutated miR165/166 target site of *PHB* (*PHBBS-GFP* or *mPHBBS-GFP*) together with *JUL1* or *JUL1(RA)* and pri-MIR165a ($n = 3–6$) (left). RNA and protein levels were determined using RT-PCR and immunoblotting, respectively (right). RbcL protein was used as the loading control. Scale bars, 200 μm. Experiment was independently repeated three times with consistent results. **b** Relative expression levels of *JUL1*, pri-MIR165a, mature miR165/166, and miR165/166 target genes (*PHB* and *REV*) were determined in *jul1 LhGR-JUL1* plants following 24-h DEX treatment ($n = 6$). **c** Relative expression levels of *JUL1*, pri-MIR165a, mature miR165/166, and miR165/166 target genes (*PHB* and *REV*) were determined in *LhGR*-amiR-*JUL1* plants following 24-h DEX treatment ($n = 6$). **d** Representative images of rosettes and individual leaves of 5-week-old Col-0, *proMIR165a:MIR165a_WT*, *proR165a:MIR165a_mut*$^{\#3}$ (top), *jul1 jul2*, *jul1 jul2 proMIR165a:MIR165a_WT*, and *jul1 jul2 proMIR165a:MIR165a_mut*$^{\#3}$ (bottom). Scale bars, 1 cm. **e** Quantification of leaf curling for the transgenic plants described in (**d**). Data are presented as box-and-whisker plots with individual data points ($n = 16$). The centre lines indicate the median, the box limits indicate the 25th percentiles and 75th percentiles, and whiskers represent the minima and maxima. **f** The ratio of mature miR165/166 to pri-MIR165a in shoot from 7 DAS Col-0, *proMIR165a:MIR165a_WT*, *proMIR165a:MIR165a_mut*$^{\#3}$, *jul1 jul2*, *jul1 jul2 proMIR165a:MIR165a_WT*, and *jul1 jul2 proMIR165a:MIR165a_mut*$^{\#3}$ seedlings ($n = 6$). The bar graphs in **a**, **b**, **c**, and **f** represent the mean ± SEM with individual data points. *n* indicates biological replicates. **b**, **c** Asterisks indicate statistically significant differences (*$P < 0.05$, **$P < 0.01$, ***$P < 0.001$) by a two-tailed Student's *t*-test. **a**, **e**, and **f** Different letters indicate statistically significant differences ($P < 0.05$), as determined by one-way ANOVA with a post hoc Tukey's HSD test. **f** Asterisks indicate statistically significant differences (*$P < 0.05$, **$P < 0.01$, ***$P < 0.001$) by one-way ANOVA with a Dunnett's test comparing each transgenic plants to their genetic background, Col-0 and *jul1 jul2*, respectively. **a**–**c** Experiments were independently repeated three times with consistent results. All experiments were independently repeated three times with consistent results. The data shown are from a representative experimental set.

environmental signals, enabling plants to adjust leaf morphology for optimal photosynthetic performance.

Methods

Plant materials and growth conditions

Arabidopsis thaliana Col-0, *jul1*, and *jul1 jul2* were used as wild-type and genetic backgrounds for the transgenic lines. The *jul1 jul2* mutants were used as described[38]. The *jul1* mutant was generated by backcrossing the *jul1 jul2* with Col-0. All seeds were germinated and grown for 1 week in a media containing 1/2 Gamborg B5 salts (Duchefa), 1% sucrose, and 0.65% phytagel (Duchefa) (pH 5.6–5.7) under long-day conditions (16 h light/8 h dark) at 21 °C. Plants for phenotypic analyses and RNA extraction were transplanted to pots at 7 days after sowing (DAS) and grown under long-day conditions. Plants for protoplast isolation were grown under short-day conditions (10 h light/14 h dark) at 21 °C and fully expanded leaves of 4-week-old plants were used.

Plasmid construction for transgenic plants and protoplast transient expression assay

To generate the *JUL1* complementation line, the *JUL1* coding sequence (CDS) was cloned into the pCAMBIA1303 vector containing 3.7 kb of the *JUL1* promoter and HA or GFP tags. To monitor the spatial expression of *MIR165a* and *JUL1*, we cloned 2.3 kb of the *MIR165a* promoter[23] or 3.7 kb of the *JUL1* promoter into the pCAMBIA1303 vector containing GUS-GFP or 3xGFP, respectively. To generate meristem specific miR165/166 suppression line, the STTM165/166 sequence[51] was cloned into the pCAMBIA1303 vector containing 1.7 kb of the RPS5A promoter[67]. To generate tissue specific *JUL1* expression lines, plasmid construction was performed using the Golden Gate cloning[68]. *JUL1-StrepII*, 3 kb of *FIL* promoter[48], 3 kb of *APL* promoter[69], and 3.7 kb of *BOP1* promoter[70] were separately PCR-amplified, and each PCR product was cloned to the universal Level 0 (Lv0) vector (pAGM9121). Lv0 vectors of *JUL1-StrepII* and various promoters were assembled to Lv1 vectors. Each Lv1 vector was assembled to an Lv2 binary vector (pAGM4723) with the antibiotic-resistant gene *BAR* containing an Lv1 vector (pICSL11017) and linker (pICH41744). To generate DEX-inducible *JUL* expression transgenic line, *JUL-StrepII* was cloned into pCR8/GW/TOPO vector. To generate DEX-inducible gene suppression transgenic line, artificial microRNA (amiR) targeting *JUL* was designed using WMD3[71]. amiR precursor was generated by overlapping PCR using pRS300 vector as a template and cloned into pCR8/GW/TOPO vector. Recombination reaction between entry vector (pCR8/GW/TOPO) and destination vector (pB7WG6SLhGR)[72] was carried out using Gateway® LR Clonase™ II enzyme mix (Invitrogen), yielding *LhGR-JUL* and *LhGR*-amiR-*JUL* constructs. All constructs were transformed into *Agrobacterium tumefaciens* GV3101, and the *Arabidopsis* plants were transformed using the *Agrobacterium* floral dipping method[73].

Protoplast expression vectors containing HA, GFP, and FLAG tags were used as templates to construct plasmids for protoplast transient expression[74]. pri-MIR165a, 24XMS2 hairpin-fused pri-MIR165a, double stranded RNA binding domain of *DCL1* (*dsRBD*)[75] were amplified by PCR and cloned into the HA vector. *PHBBS, mPHBBS* were constructed by a primer annealing and cloned into the GFP vector. The *JUL1* CDS was amplified by PCR and cloned into the FLAG vector. *mRFP-JUL1, mRFP-JUL1(RA)*, *MS2-GFP*, *JUL1-HA*, and *JUL1(RA)-HA* constructs were previously described[35]. The primers for cloning are listed in Supplementary Table 1.

Transient expression in *Arabidopsis* protoplast

For MS2 monitoring system and GFP reporter assay, 4 × 104 protoplasts were transfected with 40 μg of total plasmid DNA composed of different combinations of the vectors and incubated for 6 h at room temperature. For the cytosolic condensation of JUL1 protein, the samples were treated with 0.01% NaN_3 for 10 min. GFP and mRFP fluorescence were observed by a fluorescence microscope (LSM800, Zeiss). For RNA immunoprecipitation and pri-MIR165a processing assay, 8 × 105 protoplasts were transfected with 800 μg of total plasmid DNA for RNA immunoprecipitation and 400 μg of total plasmid DNA for pri-MIR165a processing, composed of different combinations of the vectors, respectively and incubated for 16 h at room temperature. RNA in GFP reporter assay was assessed by RT-PCR. RNAs in RNA immunoprecipitation and pri-MIR165a processing assay were measured by quantitative RT-PCR. Proteins in GFP reporter assay, RNA immunoprecipitation and pri-MIR165a processing assay were detected by horseradish peroxidase (HRP)-conjugated high-affinity anti-GFP (Santa Cruz Biotechnology) and anti-HA (Invitrogen) antibodies, respectively, and visualized using ECL solution (Pierce) and ImageQuant LAS 500 (Amersham) or X-ray film (AGFA) expose.

Recombinant protein purification

For protein purification of GST-fused recombinant proteins, GST-fused JUL1 and JUL1(RA) were expressed in *Escherichia coli* BL21 strain. Cells were grown in 500 ml of Luria broth (LB) medium at 37 °C, until they reached an optical density at 600 nm of 0.6 to 0.7 with shaking. After 1 mM isopropyl β-d-1-thiogalactopyranide (IPTG) treatment, cells were further incubated 20 h at 18 °C. The recombinant GST-fused proteins were purified by Glutathione Sepharose 4B (Cytiva) according to the manufacturer's protocol. GST-fused JUL1 and JUL1(RA) vectors were previously described[35].

RNA isolation and quantitative RT-PCR (qRT-PCR)

Total RNAs from shoots of 7-day-after-sowing (DAS) seedlings, leaves of 5-week-old plants, and mesophyll protoplasts of 4-week-old plants were isolated using TRIzol reagent (Invitrogen) according to the manufacturer's instructions. Reverse transcription of mRNAs and pri-MIR165/166 was carried out with 1 μg of total RNA, oligo(dT) primers, and ImProm-II reverse transcriptase (Promega) according to the manufacturer's instructions. Reverse transcription of mature miR165/166 was carried out with 1 μg of total RNA, miR165/166-specific stem loop primer, and Superscript III reverse transcriptase (Invitrogen) by pulsed reverse transcription[76]. qRT-PCR was performed with CFX Connect Real-Time System (BIO-RAD) and the SYBR Premix ExTaq system (Takara) according to the manufacturer's instructions. Primers for qRT-PCR are listed in Supplementary Table 1.

Circular dichroism (CD) assay

CD assay was adoted with minor modification from the previous study[35]. All CD spectra were obtained from a J-815 CD Spectrometer (Jasco) at 25 °C using quartz cuvettes with a 2.0 mm path length. Each spectrum was recorded over a wavelength range of 220 nm to 320 nm with a 50 nm min^{-1} scanning speed. The final spectrum encompassed the average of five scans of the same sample. Synthesized RNA oligonucleotides (2 μM) were slowly cooled from 95 °C to room temperature in a binding buffer [10 mM Tris-HCl (pH 8.0) and 1 mM $MgCl_2$, either in the absence or presence of 100 mM KCl] to reach equilibrium prior to CD measurements. The re-natured RNA oligonucleotides containing the 100 mM KCl were combined with 1 μM JUL1 protein and incubated for 30 min before the CD measurement to observe the G-quadruplex structure of the RNA in the pri-MIR165a–JUL1 complex. To eliminate the influence of proteins and buffers, the spectra containing the JUL1 protein were corrected using 1 μM JUL1 in buffer as a baseline. The spectra of 1 μM JUL1 alone were also recorded to demonstrate that JUL1 has no significant effect on the spectrum of the RNA G-quadruplex.

RNA Electrophoretic mobility shift (REMSA) assay

RNA EMSA was adopted with minor modifications from the previous study[35]. For RNA EMSA with G-rich element, single-stranded RNA (ssRNA) oligonucleotides of the G-rich region of primary MIR165a (pri-MIR165a_G-rich), various G to A mutants (mut^{ALL}, $mut^{\#1}$, $mut^{\#2}$, and $mut^{\#3}$) and anti sensed counter part of G-rich element (anti-probe) were synthesized (Bioneer). For RNA EMSA of pri-MIR165a, full-length pri-MIR165a RNA was produced by in vitro transcription using DNA template, which was generated from PCR amplification of full-length pri-MIR165a containing the minimal T7 promoter. Transcription was carried out using the RiboMAX RNA Production System-T7 (Promega). Transcribed RNA was denatured and purified by gel electrophoresis using a 12% urea-TBE gel. RNA probes were labelled with [γ–^{32}P]-ATP (10 mCi ml^{-1}) by incubation with T4 polynucleotide kinase (New England Biolabs) for 30 min at 37 °C. The unlabeled radionucleotides were removed using an Illustra MicroSpin G25 column (Amersham). Radioisotope-labelled RNA probes were denatured by incubation at 95 °C for 5 min and rapidly cooled on ice. 0–40 μM of GST-JUL1, GST-JUL1(RA) proteins were incubated in a binding buffer [10 mM Tris-HCl (pH 8.0), 2.5% glycerol, 0.5 mM 1,4-dithiothreitol (DTT), 50 μg ml^{-1} BSA, 100 mM KCl, 250 μM EDTA, and 1 μg heparin] with 10 nM RNA probes for 20 minutes at room temperature. The reaction mixture was resolved on a 6–12% polyacrylamide gel in 0.5× TBE buffer. Gels were visualized on a Phosphor screen using a Typhoon FLA 9000 PhosphorImager (GE Healthcare). RNA probes for RNA EMSA and primers for template amplification are listed in Supplementary Table 1.

Nuclear protein extraction

Sucrose gradient subcellular fractionation was performed as previously described with minor modification[77]. Briefly, *YPF-DCL1* expressing *Arabidopsis* protoplasts were suspended in cell lysis buffer [20 mM Tris-Cl (pH7.5), 250 mM Sucrose, 2.5 mM $MgCl_2$, 25% glycerol, 20 mM KCl, 2 mM EDTA, 1% Triton X-100, 1 mM PMSF, 5 mM DTT, and protease inhibitor (PI; Roche)] and the nuclei is pelleted by centrifugation at 1500 × *g* for 10 min at 4 °C. This pellet was gently washed 4 times with cell lysis buffer. Washed pellets were resuspended in nuclei resuspension buffer 1 [20 mM Tris-Cl (pH7.5), 250 mM Sucrose, 10 mM $MgCl_2$, 0.5% Triton X-100, 5 mM 2-mrcaptoethanol (BME), 1 mM PMSF, and PI]. The suspension was layered on the top of equal volume of nuclei resuspension buffer 2 [20 mM Tris-Cl (pH 7.5), 10 mM $MgCl_2$, 1.7 M sucrose, 0.5% Triton X-100, 5 mM BME, 1 mM PMSF, and PI] and centrifuged at 16,000 × *g* for 45 min at 4 °C. The supernatant was removed, and the pellet was lysed with nuclei lysis buffer [50 mM Tris-Cl (pH 7.5), 10 mM EDTA, 0.05% SDS, 0.1% Triton X-100, and PI] to obtain the nuclear fraction. The nuclear fraction was used for the in vitro pri-MIRNA processing assay.

In vitro pri-MIRNA processing assay

In vitro pri-MIRNA processing assay was performed as previously described with minor modifications[75]. Transcription was carried out with the DNA template of pri-MIR165a described above using the RiboMAX Large Scale RNA Production System-T7 (Promega) in the presence of [α–^{32}P]-UTP (10 mCi ml^{-1}), and the RNA probes were denatured and purified by gel electrophoresis using a 12% urea-TBE gel. 100 nM of pri-MIR165a RNA probes were incubated with an activity buffer [20 mM Tris-HCl (pH 7.0), 50 mM NaCl, 4 mM $MgCl_2$, 5 mM ATP, and 1 mM GTP] and 2 U $μl^{-1}$ RNasin RNase inhibitor (Promega) for 40 min at 37 °C, in the absence or presence of 2.5 μM of GST-DCL1 and 0 to 20 μM of GST-JUL1. After incubation, proteinase K (NEB) was added and incubated for 15 min. For gel electrophoresis, the samples were mixed with RNA Gel Loading Dye (Thermo Scientific), incubated at 95 °C for 5 min and cooled on ice. The incubated samples were separated on a 12% urea-TBE gel, fixed by fixation solution (20% ethanol and 5% acetic acid), and visualized on a Phosphor screen using a Typhoon FLA 9000 PhosphorImager (GE Healthcare).

RNA immunoprecipitation

RNA immunoprecipitation was adopted with minor modifications from the previous study[35]. 1 mg of 4-week-old Col-0 and *jul1 pro-JUL1:JUL1-HA* leaves or 8 × 105 protoplasts were used for RNA immunoprecipitation sample. Cross-linking was done for 15 min with 1% formaldehyde under vacuum. After quenching with 0.125 M glycine for 10 min and brief rinse with 1x PBS (pH7.4), leaves were frozen in liquid nitrogen and ground to fine powder. RNA-protein complexes in ground leaves were extracted using IP buffer [100 mM KCl, 2.5 mM $MgCl_2$, 10 mM Tris-HCl (pH 8.0), 10% glycerol, 0.5% NP-40, 1 mM DTT, 100 U ml^{-1} RNasin RNase inhibitor (Promega), 25 μM MG132, and PI (Mini-complete tablet, Roche)]. After centrifugation at 13,000 × *g* for 10 minutes at 4 °C, 300 μl of cell extracts were incubated with 1 μg of HA antibody (Roche) for overnight at 4 °C with gentle rotation. A 30 μl aliquot of the cell extracts was stored at −80 °C for later experiments. Dynabeads Protein G magnetic beads (Invitrogen) were washed three times in a washing buffer [100 mM KCl, 2.5 mM $MgCl_2$, 10 mM Tris-HCl (pH 8.0), 10% glycerol, 0.5% NP-40, and 100 U ml^{-1} RNasin RNase inhibitor (Promega)], then the anti-HA-decorated extracts were incubated with 10 μl Protein G magnetic beads for 2 h at 4 °C with gentle rotation. The beads were then washed eight times with the washing buffer. Co-immunoprecipitated RNAs were isolated by TRIzol reagent (Invitrogen) and reverse transcription was carried out using SuperScript III (Invitrogen) according to the manufacturer's instruction. Co-immunoprecipitated RNAs were analyzed by qRT-PCR and proteins were detected by horseradish peroxidase (HRP)-conjugated high-affinity anti-HA (Invitrogen) and anti-FLAG (Cell Signaling Technology) antibodies and visualized using ECL solution (Pierce) and ImageQuant LAS 500

(Amersham) or X-ray film (AGFA) expose. The primers for RNA immunoprecipitation are listed in Supplementary Table 1.

Bead surface binding assay

ssRNA oligonucleotides of the 5′ biotinylated and 3′ Cy5-labeled G-rich element (5′-[biotin]UUGAGGGGAAUGUUGUCUGGAU[Cy5]–3′) and 5′ Cy3-labeled anti-probe (5′-[Cy3]UCGGACCAGGCUUCAUCCCCCCCAA-3′) were synthesized (Bioneer). The RNA probes, with a concentration of 25 μM, were heated in a structure buffer [10 mM Tris-HCl (pH 8.0), 100 mM KCl, and 1 mM $MgCl_2$] at 95 °C for 5 min and then gradually cooled to 25 °C. NeutrAvidin Agarose Resin beads (Invitrogen) were washed twice with the structure buffer and incubated with 2.5 μM of the G-rich element for 1 h at 4 °C. The RNA-bead complexes were washed twice with the structure buffer. In the absence or presence of 25 μM of GST-JUL or GST-JUL1(RA) proteins, 250 nM of anti-probe was added to RNA-bead complexes and incubated for 10 min at room temperature with occasional mixing. Cy3 and Cy5 fluorescence signals were observed with a confocal microscope (LSM800, Carl Zeiss). Cy3 and Cy5 were excited at the wavelengths of 488 nm and 640 nm, respectively. The emission wavelengths for Cy3 and Cy5 fluorescence were recorded at 400–640 nm and 650–700 nm, respectively. The RNA probes for bead binding assay are listed in Supplementary Table 1.

Förster resonance energy transfer (FRET) analysis

The ssRNA oligonucleotides in the bead surface binding assay were also utilized in the FRET analysis. The RNA probes, with a concentration of 25 μM, were heated in a structure buffer [10 mM Tris-HCl (pH 8.0), 100 mM KCl, and 1 mM $MgCl_2$] at 95 °C for 5 min and then gradually cooled to 25 °C. The G-rich element was incubated overnight at 4 °C with GST-JUL1 or GST-JUL1(RA). The anti-probe was then added to RNA-protein mixture and incubated for 30 minutes at room temperature with occasional mixing. The final concentrations of each RNA probes and proteins were set to 2.5 μM and 25 μM, respectively. Fluorescence intensities of Cy3 and Cy5 were measured using a SYNERGY H1 multi-mode microplate reader (BioTek). The sample was excited at 520 nm, and the fluorescence emission intensity at 660 nm divided by the emission intensity at 560 nm was presented as a FRET ratio[78]. The RNA probes for FRET analysis are listed in Supplementary Table 1.

Adaxial–abaxial phenotypic analysis

The stem cross-section was performed as previously reported[79]. For stem cross section, 0.5-cm long sections of the inflorescence stem were harvested from the base when stem length was 20 cm and embedded in Spurr's resin (Sigma-Aldrich), following the manufacturer's instructions. Embedded stem samples were sectioned into 0.2 μm thickness using sliding microtome (RM2265, Leica). Cross-section images of stem samples were acquired using a light microscopy (Axioplan2, Carl Zeiss). Relative areas of the central and peripheral regions were calculated as the ratio of each region's area to the total stem area. Transverse section of the mid-vein in leaf blades and petioles followed procedures as described previously[80]. Seventh leaves harvested at 21 DAS were embedded in Technovit 7100 resin (Kulzer Technik), following the manufacturer's instructions. Embedded leaf samples were sectioned into 4 μm thickness using a rotary microtome (Microtome HM 325, Thermo Scientific). Transverse-section images of leaves were acquired using a light microscopy (Carl Zeiss). Relative areas of xylem and phloem in mid-vein and petiole were calculated as the ratio of the area of xylem or phloem to the sum of xylem and phloem areas. Leaf and rosette phenotypes were observed at 28 DAS. To assess the extent of leaf curling, the visible curled areas and the flattened leaf areas were measured as described previously[49]. The visible curled leaf areas were estimated from photographs taken directly above the specimens. For the flattened leaf areas, same leaves are flattened under clear adhesive tape and photographed. ImageJ[81] was used to calculate relative areas of central, peripheral, phloem, xylem, curled leaf, and flattened leaf region.

GUS staining

Seedlings at 7, 14, and 21 DAS were first cleared with 90% acetone for 1 h at 4 °C. Following a rinse with a phosphate buffer (pH 7.2), the cleared tissues were incubated overnight with GUS substrate solution [50 mM phosphate buffer (pH 7.0), 2.5 mM potassium ferrocyanide, 2.5 mM potassium ferricyanide, 0.1% Triton-X, 10 mM EDTA, 1 mg/ml 5-bromo-4-chloro-3-indolyl-β-d-glucuronidase (X-Gluc)] at 37 °C. Subsequently, remained chlorophyll in GUS-stained seedlings was removed with 70% ethanol.

RG4 analysis in *Arabidopsis* protein coding RNA, pre-MIRNA, lncRNA, and tRNA

Arabidopsis pre-MIRNA, lncRNA, tRNA, and protein coding RNA sequences were retrieved from miRbase (https://www.mirbase.org/)[43], PLncDB (https://www.tobaccodb.org/plncdb/)[82], tRex (http://combio.pl/trex)[83], and TAIR10 (https://www.arabidopsis.org/), respectively. Probabilities of G-quadruplex formation (G-score) of *Arabidopsis* coding and non-coding RNA sequences were calculated from QGRS Mapper[84]. To analyze the putative minimal JUL1-binding sequence, RNA sequences were enriched by systematic evolution of ligands by exponential enrichment (SELEX)[35]. After enrichment, RNA sequences were analyzed by Multiple Em for Motif Elicitation (MEME; version 5.4.1)[41] with following parameters [-rna -nostatus -mod zoops -nmotifs 5 -minw 6 -maxw 9 -objfun classic -markov_order 0].

Multiple alignments of pre-MIRNA165/166 family sequences across plant species

Pre-MIRNA165/166 family sequences of *Populus trichocarpa*, *Arabidopsis thaliana*, *Oryza sativa*, *Selaginella moellendorffii*, and *Physcomitrium patens* were retrieved from miRbase[43]. Multiple alignments of pre-MIRNA165/166 family sequences were conducted using CLUSTAL W with default options in MEGA11[85] and visualized using Unipro UGENE[86].

Stem-loop structure prediction of pri-MIR165a

Arabidopsis pri-MIR165a sequence was retrieved from miRex2.0 (http://www.combio.pl/mirex2)[87] and stem-loop structure of pri-MIR165a was predicted using RNAfold web server (http://rna.tbi.univie.ac.at//cgi-bin/RNAWebSuite/RNAfold.cgi)[88] with default options.

Statistical analyses

Statistical analyses of data were conducted using GraphPad Prism 9.0.

Reporting summary

Further information on research design is available in the Nature Portfolio Reporting Summary linked to this article.

Data availability

Data are available within the Article, Supplementary Information or Source Data file. Source data are provided with this manuscript. Source data are provided with this paper.

References

1. Tsukaya, H. Leaf development. *Arab. Book/Am. Soc. Plant Biol.* **11**, e0163 (2013).
2. Kalve, S., De Vos, D. & Beemster, G. T. S. Leaf development: a cellular perspective. *Front. Plant Sci.* **5**, https://doi.org/10.3389/fpls.2014.00362 (2014).
3. Taiz, L., Zeiger, E., Møller, I. M. & Murphy, A. *Plant Physiology and Development:6th Revised Edition* (SINAUER Associates Inc., 2014).

4. Kenrick, P. & Crane, P. R. The origin and early evolution of plants on land. *Nature* **389**, 33–39 (1997).
5. Pillitteri, L. J., Guo, X. & Dong, J. Asymmetric cell division in plants: mechanisms of symmetry breaking and cell fate determination. *Cell. Mol. Life Sci.* **73**, 4213–4229 (2016).
6. Fukushima, K. & Hasebe, M. Adaxial-abaxial polarity: The developmental basis of leaf shape diversity. *Genesis* **52**, 1–18 (2014).
7. Caggiano, M. P. et al. Cell type boundaries organize plant development. *eLife* **6**, e27421 (2017).
8. Scacchi, E. et al. A diffusible small-RNA-based Turing system dynamically coordinates organ polarity. *Nat. Plants* **10**, 412–422 (2024).
9. Burian, A. et al. Specification of leaf dorsiventrality via a pre-patterned binary readout of a uniform auxin input. *Nat. Plants* **8**, 269–280 (2022).
10. Scarpella, E., Barkoulas, M. & Tsiantis, M. Control of leaf and vein development by auxin. *Cold Spring Harbor Perspect. Biol.* **2** https://doi.org/10.1101/cshperspect.a001511 (2010).
11. Kneuper, I. et al. Auxin biosynthesis and cellular efflux act together to regulate leaf vein patterning. *J. Exp. Bot.* **72**, 1151–1165 (2021).
12. Szakonyi, D., Moschopoulos, A. & Byrne, M. E. Perspectives on leaf dorsoventral polarity. *J. Plant Res.* **123**, 281–290 (2010).
13. Husbands, A. Y., Chitwood, D. H., Plavskin, Y. & Timmermans, M. C. P. Signals and prepatterns: new insights into organ polarity in plants. *Genes Dev.* **23**, 1986–1997 (2009).
14. Manuela, D. & Xu, M. Patterning a leaf by establishing polarities. *Front. Plant Sci.* **11**, 568730 (2020).
15. Scarpella, E. Leaf vein patterning. *Annu. Rev. Plant Biol.* **75**, 377–398 (2024).
16. Zhang, Y. et al. Divergence of three *BRX* homoeologs in *Brassica rapa* and its effect on leaf morphology. *Hortic. Res.* **8**, 68 (2021).
17. Guo, Y., Qin, G., Gu, H. & Qu, L.-J. *Dof5.6/HCA2*, a dof transcription factor gene, regulates interfascicular cambium formation and vascular tissue development in *Arabidopsis*. *Plant Cell* **21**, 3518–3534 (2009).
18. Tasaka, M. From central–peripheral to adaxial–abaxial. *Trends Plant Sci.* **6**, 548–550 (2001).
19. Kerstetter, R. A. et al. KANADI regulates organ polarity in *Arabidopsis*. *Nature* **411**, 706–709 (2001).
20. Emery, J. F. et al. Radial patterning of *Arabidopsis* shoots by class III HD-ZIP and KANADI gGenes. *Curr. Biol.* **13**, 1768–1774 (2003).
21. Dengler, N. & Kang, J. Vascular patterning and leaf shape. *Curr. Opin. Plant Biol.* **4**, 50–56 (2001).
22. Ilegems, M. et al. Interplay of auxin, KANADI and Class III HD-ZIP transcription factors in vascular tissue formation. *Development* **137**, 975–984 (2010).
23. Carlsbecker, A. et al. Cell signalling by microRNA165/6 directs gene dose-dependent root cell fate. *Nature* **465**, 316–321 (2010).
24. Besnard, F., Vernoux, T. & Hamant, O. Organogenesis from stem cells *in planta*: multiple feedback loops integrating molecular and mechanical signals. *Cell. Mol. Life Sci.* **68**, 2885–2906 (2011).
25. Daniela Cordeiro, S., Canhoto, J. & Correia, S. Regulatory non-coding RNAs: Emerging roles during plant cell reprogramming and *in vitro* regeneration. *Front. Plant Sci.* **13** https://doi.org/10.3389/fpls.2022.1049631 (2022).
26. Yadav, A., Mathan, J., Dubey, A. K. & Singh, A. The emerging role of non-coding RNAs (ncRNAs) in plant growth, development, and stress response signaling. *Non-coding RNA* **10** https://doi.org/10.3390/ncrna10010013 (2024).
27. Zhou, G. K. et al. Overexpression of miR165 affects apical meristem formation, organ polarity establishment and vascular development *in Arabidopsis*. *Plant Cell Physiol.* **48**, 391–404 (2007).
28. Merelo, P. et al. Regulation of *MIR165/166* by class II and class III homeodomain leucine zipper proteins establishes leaf polarity. *Proc. Natl. Acad. Sci. USA* **113**, 1973–11978 (2016).
29. Zhou, Y. et al. Spatiotemporal sequestration of miR165/166 by *Arabidopsis* argonaute10 promotes shoot apical meristem maintenance. *Cell Rep.* **10**, 1819–1827 (2015).
30. Garcia, D., Collier, S. A., Byrne, M. E. & Martienssen, R. A. Specification of leaf polarity in *Arabidopsis* via the trans-acting siRNA pathway. *Curr. Biol.* **16**, 933–938 (2006).
31. Fahlgren, N. et al. Regulation of *AUXIN RESPONSE FACTOR3* by *TAS3* ta-siRNA affects developmental timing and patterning in *Arabidopsis*. *Curr. Biol.* **16**, 939–944 (2006).
32. Zhan, J. & Meyers, B. C. Plant small RNAs: their biogenesis, regulatory roles, and functions. *Annu. Rev. Plant Biol.* **74**, 21–51 (2023).
33. Yu, Y., Zhang, Y., Chen, X. & Chen, Y. Plant noncoding RNAs: hidden players in development and stress responses. *Annu. Rev. Cell Dev. Biol.* **35**, 407–431 (2019).
34. Wierzbicki, A. T., Blevins, T. & Swiezewski, S. Long noncoding RNAs in plants. *Annu. Rev. Plant Biol.* **72**, 245–271 (2021).
35. Cho, H. et al. Translational control of phloem development by RNA G-quadruplex-JULGI determines plant sink strength. *Nat. Plants* **4**, 376–390 (2018).
36. Nam, H. et al. JULGI-mediated increment in phloem transport capacity relates to fruit yield in tomato. *Plant Biotechnol. J.* **20**, 1533–1545 (2022).
37. Wallner, E. S. et al. Strigolactone- and karrikin-independent SMXL proteins are central regulators of phloem formation. *Curr. Biol.* **27**, 1241–1247 (2017).
38. Park, C. et al. Evolution of the *JULGI–SMXL4/5* module for phloem development in angiosperms. *Proc. Natl. Acad. Sci. USA* **122**, e2416674122 (2025).
39. Mullen, M. A. et al. RNA G-Quadruplexes in the model plant species *Arabidopsis thaliana*: prevalence and possible functional roles. *Nucleic Acids Res.* **38**, 8149–8163 (2010).
40. Sanchez-Diaz, P. & Penalva, L. O. F. Post-transcription meets post-genomic: the saga of RNA binding proteins in a new era. *RNA Biol.* **3**, 101–109 (2006).
41. Bailey, T. L., Johnson, J., Grant, C. E. & Noble, W. S. The MEME suite. *Nucleic Acids Res.* **43**, W39–W49 (2015).
42. Zhang, R. et al. Whole genome identification of potential G-quadruplexes and analysis of the G-quadruplex binding domain for SARS-CoV-2. *Front. Genet.* **11**, 587829 (2020).
43. Kozomara, A., Birgaoanu, M. & Griffiths-Jones, S. miRBase: from microRNA sequences to function. *Nucleic Acids Res.* **47**, D155–D162 (2019).
44. Song, X., Li, Y., Cao, X. & Qi, Y. MicroRNAs and their regulatory roles in plant-environment interactions. *Annu. Rev. Plant Biol.* **70**, 489–525 (2019).
45. McConnell, J. R. et al. Role of *PHABULOSA* and *PHAVOLUTA* in determining radial patterning in shoots. *Nature* **411**, 709–713 (2001).
46. Mallory, A. C. et al. MicroRNA control of *PHABULOSA* in leaf development: Importance of pairing to the microRNA 5′ region. *EMBO J.* **23**, 3356–3364 (2004).
47. Liu, Z., Jia, L., Wang, H. & He, Y. HYL1 regulates the balance between adaxial and abaxial identity for leaf flattening via miRNA-mediated pathways. *J. Exp. Bot.* **62**, 4367–4381 (2011).
48. Tameshige, T. et al. Pattern dynamics in adaxial-abaxial specific gene expression are modulated by a plastid retrograde signal during *Arabidopsis thaliana* Leaf Development. *PLoS Genet.* **9**, https://doi.org/10.1371/journal.pgen.1003655 (2013).
49. Whitley, P., Hinz, S. & Doughty, J. Arabidopsis FAB1/PIKfyve proteins are essential for development of viable pollen. *Plant Physiol.* **151**, 1812–1822 (2009).
50. Yan, J. et al. Effective small RNA destruction by the expression of a short tandem target mimic in *Arabidopsis*. *Plant Cell* **24**, 415–427 (2012).

51. Tang, G. et al. Construction of short tandem target mimic (STTM) to block the functions of plant and animal microRNAs. *Methods* **58**, 118–125 (2012).
52. Tenorio Berrío, R. et al. Single-cell transcriptomics sheds light on the identity and metabolism of developing leaf cells. *Plant Physiol.* **188**, 898–918 (2022).
53. Bertrand, E. et al. Localization of *ASH1* mRNA particles in living Yeast. *Mol. Cell* **2**, 437–445 (1998).
54. Reinhart, B. J. et al. MicroRNAs in plants. *Genes Dev.* **16**, 1616–1626 (2002).
55. Park, W. et al. CARPEL FACTORY, a dicer homolog, and HEN1, a novel protein, act in microRNA metabolism in *Arabidopsis thaliana*. *Curr. Biol.* **12**, 1484–1495 (2002).
56. Loughlin, F. E. et al. The zinc fingers of the SR-like protein ZRANB2 are single-stranded RNA-binding domains that recognize 5′ splice site-like sequences. *Proc. Natl. Acad. Sci. USA* **106**, 5581–5586 (2009).
57. Lucas, W. J. et al. The plant vascular system: evolution, development and functions. *J. Integr. Plant Biol.* **55**, 294–388 (2013).
58. Yu, Y. et al. ARGONAUTE10 promotes the degradation of miR165/6 through the SDN1 and SDN2 exonucleases in Arabidopsis. *PLoS Biol.* **15**, e2001272 (2017).
59. Zhang, C. et al. Regulation of ARGONAUTE10 expression enables temporal and spatial precision in axillary meristem initiation in arabidopsis. *Dev. Cell* **55**, 603–616.e5 (2020).
60. Husbands, A. Y., Benkovics, A. H., Nogueira, F. T. S., Lodha, M. & Timmermans, M. C. P. The ASYMMETRIC LEAVES complex employs multiple modes of regulation to affect adaxial-abaxial patterning and leaf complexity. *Plant Cell* **27**, 3321–3335 (2015).
61. Prigge, M. J. et al. Class III homeodomain-leucine zipper gene family members have overlapping, antagonistic, and distinct roles in arabidopsis development. *Plant Cell* **17**, 61–76 (2005).
62. Yip, H. K., Floyd, S. K., Sakakibara, K. & Bowman, J. L. Class III HD-Zip activity coordinates leaf development in *Physcomitrella patens*. *Dev. Biol.* **419**, 184–197 (2016).
63. Floyd, S. K., Zalewski, C. S. & Bowman, J. L. Evolution of class III homeodomain-leucine zipper genes in streptophytes. *Genetics* **173**, 373–388 (2006).
64. Tatematsu, K. et al. A molecular mechanism that confines the activity pattern of miR165 in Arabidopsis leaf primordia. *Plant J.* **82**, 596–608 (2015).
65. Yang, T. et al. The interaction between miR160 and miR165/166 in the control of leaf development and drought tolerance in *Arabidopsis*. *Sci. Rep.* **9**, 2832 (2019).
66. Sun, S. et al. Sweet potato NAC transcription factor *NAC43* negatively regulates plant growth by causing leaf curling and reducing photosynthetic efficiency. *Front. Plant Sci.* **14**, https://doi.org/10.3389/fpls.2023.1095977 (2023).
67. Maruyama, D. et al. Independent control by each female gamete prevents the attraction of multiple pollen tubes. *Dev. Cell* **25**, 317–323 (2013).
68. Weber, E. et al. A modular cloning system for standardized assembly of multigene constructs. *PLoS ONE* **6**, e16765 (2011).
69. Bonke, M. et al. APL regulates vascular tissue identity in Arabidopsis. *Nature* **426**, 181–186 (2003).
70. McKim, S. M. et al. The *BLADE-ON-PETIOLE* genes are essential for abscission zone formation in *Arabidopsis*. *Development* **135**, 1537–1546 (2008).
71. Ossowski, S., Schwab, R. & Weigel, D. Gene silencing in plants using artificial microRNAs and other small RNAs. *Plant J.* **53**, 674–690 (2008).
72. Kang, N. Y., Cho, C. & Kim, J. Inducible expression of *Arabidopsis Response Regulator 22* (*ARR22*), a Type-C *ARR*, in transgenic arabidopsis enhances drought and freezing tolerance. *PLoS ONE* **8**, e79248 (2013).
73. Clough, S. J. & Bent, A. F. Floral dip: a simplified method for *Agrobacterium*-mediated transformation of *Arabidopsis thaliana*. *Plant J.* **16**, 735–743 (1998).
74. Nam, H. et al. CPR5-mediated nucleo-cytoplasmic localization of IAA12 and IAA19 controls lateral root development during abiotic stress. *Proc. Natl. Acad. Sci. USA* **120**, e2209781120 (2023).
75. Dong, Z., Han, M.-H. & Fedoroff, N. The RNA-binding proteins HYL1 and SE promote accurate in vitro processing of pri-miRNA by DCL1. *Proc. Natl. Acad. Sci. USA* **105**, 9970–9975 (2008).
76. Varkonyi-Gasic, E. & Hellens, R. P. Quantitative stem-loop RT-PCR for detection of microRNAs. *Methods Mol. Biol.* **744**, 145–157 (2011).
77. Park, J. et al. The HIGH EXPRESSION OF OSMOTICALLY RESPONSIVE GENE15–HISTONE DEACETYLASE9 complex associates with HYPONASTIC LEAVES 1 to modulate microRNA expression in response to abscisic acid signaling. *Plant Cell* **35**, 2910–2928 (2023).
78. Kopp, M. C. et al. In vitro FRET analysis of IRE1 and BiP association and dissociation upon endoplasmic reticulum stress. *eLife* **7**, e30257 (2018).
79. Han, S. et al. BIL1-mediated MP phosphorylation integrates PXY and cytokinin signalling in secondary growth. *Nat. Plants* **4**, 605–614 (2018).
80. Jun, S. E. et al. AtELP4 a subunit of the Elongator complex in *Arabidopsis*, mediates cell proliferation and dorsoventral polarity during leaf morphogenesis. *Front. Plant Sci.* **13**, 1033358 (2022).
81. Abramoff, M., Magalhães, P. & Ram, S. J. Image processing with imageJ. *Biophoton. Int.* **11**, 36–42 (2003).
82. Jin, J. et al. PLncDB V2.0: a comprehensive encyclopedia of plant long noncoding RNAs. *Nucleic Acids Res.* **49**, D1489–D1495 (2021).
83. Thompson, A. et al. tRex: a web portal for exploration of tRNA-derived fragments in *Arabidopsis thaliana*. *Plant Cell Physiol.* **59**, e1–e1 (2018).
84. Kikin, O., D'Antonio, L. & Bagga, P. S. QGRS mapper: a web-based server for predicting G-quadruplexes in nucleotide sequences. *Nucleic Acids Res.* **34**, W676–W682 (2006).
85. Tamura, K., Stecher, G. & Kumar, S. MEGA11: molecular evolutionary genetics analysis version 11. *Mol. Biol. Evol.* **38**, 3022–3027 (2021).
86. Rose, R. et al. Flexible design of multiple metagenomics classification pipelines with UGENE. *Bioinformatics* **35**, 1963–1965 (2019).
87. Zielezinski, A. et al. mirEX 2.0 - an integrated environment for expression profiling of plant microRNAs. *BMC Plant Biol.* **15**, 144 (2015).
88. Gruber, A. R. et al. The vienna RNA websuite. *Nucleic Acids Res.* **36**, W70–W74 (2008).

Acknowledgements

We appreciate Prof. Seung-Yeol Park (POSTECH) and Prof. Seong Wook Yang (Yonsei University) for technical advice and useful suggestions. This work was supported by grants to I.H. from the National Research Foundation of Korea (NRF) grant funded by the Ministry of Science and ICT, Republic of Korea (RS-2025-14342984); and from the New Breeding Technologies Development Program, Republic of Korea (RS-2024-00322420). H.S.C. was supported by the Basic Science Research Program through the NRF funded by the Ministry of Education, Republic of Korea (RS-2023-00276750 and RS-2024-00461525). G-T.K. was supported by the Basic Science Research Program through the NRF funded by the Ministry of Education, Republic of Korea (RS-2020-NR049596).

Author contributions

S.P., H.S.C., and I.H. conceived and supervised this study; S.P., H.S.C., S.L., Y.L., and I.H. designed the experiments; S.P., H.S.C., S.L., S.E.J., and G-T.K. performed the experiments and the data analysis; S.P., C.P., H.S.C., S.C., and H.L. generated plasmid constructs and transgenic plants; S.P., H.S.C., and I.H. wrote the original draft; and all authors reviewed and edited the manuscript.

Competing interests
The authors declare no competing interests.

Additional information
Supplementary information The online version contains supplementary material available at https://doi.org/10.1038/s41467-025-67339-7.

Correspondence and requests for materials should be addressed to Ildoo Hwang.

Peer review information *Nature Communications* thanks Xiaofei Yang and the other anonymous reviewer(s) for their contribution to the peer review of this work. A peer review file is available.